Int. J. Heat Mass Transfer. Vol. 36, No. 1, pp. 213–226, 1993
Printed in Great Britain

0017-9310/93 $5.00 + 0.00

A study of circumferentially-heated and block-heated heat pipes—II. Three-dimensional numerical modeling as a conjugate problem

JOSEPH SCHMALHOFER and AMIR FAGHRI
Department of Mechanical and Materials Engineering, Wright State University, Dayton, OH 45435, U.S.A.

(*Received* 12 *August* 1991 *and in final form* 25 *November* 1991)

Abstract—A general three-dimensional numerical heat pipe model which includes the pipe wall, wick, and vapor flow as a conjugate heat transfer problem has been developed. The model was employed to solve for the operating characteristics of a circumferentially-heated and block-heated heat pipe. These numerical results were compared with experimental data from the heat pipe described in Part I. A good agreement between the experimental data and the numerical results was obtained for both heating modes.

1. INTRODUCTION

THE THREE-DIMENSIONAL numerical solution of block-heated heat pipes as a conjugate problem has not been performed in the past due to the complexity of the problem. Circumferentially-heated cylindrical heat pipes have been modeled numerically in two dimensions using cylindrical coordinates for steady-state [1] and transient [2] conditions. The evaporator region of a block-heated cylindrical heat pipe has been modeled numerically by assuming that the pipe diameter is significantly larger than the wall thickness and the heated region is much longer than its width [3, 4]. These assumptions allowed the circumference of the evaporator to be modeled in Cartesian coordinates.

Rosenfeld [3] developed analytical and numerical methods to determine the steady-state wall temperature profile in the azimuthal direction for a block-heated heat pipe using a power-law assumption to represent the boiling of the working fluid. The geometry of the model was a cylindrical pipe with evaporator and condenser sections and no adiabatic transport section. A narrow block heater was placed along the axial direction. It was assumed that the evaporator length was much longer than its width and, for the closed-form analytical model, that the temperature difference across the wall in the radial direction was negligible because the wall was thin and had a high thermal conductivity. It was also assumed that the vapor temperature was uniform and constant. It was stated that the exponent of the power-law used to model the boiling of the working fluid can vary from 0.5 to 6.0 for different wall materials and thicknesses, although values between 1.0 and 2.0 are most common. The closed-form analytical model of the evaporator region was developed using a one-dimensional Cartesian coordinate system to represent the azimuthal direction. Two different sets of boundary conditions were applied. The first case applied to heat pipes with large diameters, thin walls, and low wall thermal conductivities and was solved analytically by simple integration. The second case pertained to thick walls and high thermal conductivities, resulting in a boundary-value problem which was solved using the shooting method.

Cao *et al.* [4] numerically analyzed the outside wall temperature profile in the evaporator section of high- and low-temperature cylindrical heat pipes with localized heating under steady-state conditions. The evaporator for the high-temperature heat pipe was a point source (spot-heated) with the remainder of the heat pipe operating as the condenser. The low-temperature heat pipe consisted of a block-heated evaporator that covered a larger portion of the circumference than the spot heater, a short adiabatic transport region and a circumferential condenser. The vapor temperature was assumed constant throughout the entire vapor space. The diameter of the heat pipe was assumed to be much larger than the wall thickness, thus allowing a two-dimensional Cartesian coordinate system to represent the axial and azimuthal directions. The finite-difference method based on the control-volume formulation was used to solve the two-dimensional energy conservation equation. It was determined that for high-temperature spot-heated heat pipes, the thermal conductivity of the wall played an important role in limiting the peak wall temperature directly underneath the heater.

Chen and Faghri [1] numerically analyzed the steady-state operating characteristics of circumferentially-heated cylindrical heat pipes with single or multiple heat sources using a two-dimensional conjugate heat

NOMENCLATURE

A_c	outer surface area of condenser section [m^2]
A_e	outer surface area of evaporator section [m^2]
C	ratio of the screen mesh wire diameter to the opening width of the screen, d/w_s
C_p	specific heat [J kg^{-1} K^{-1}]
D	ratio of the screen mesh wire diameter to the wick thickness, d/t_w
d	screen mesh wire diameter [m]
h_{fg}	latent heat [J kg^{-1}]
k	thermal conductivity [W m^{-1} K^{-1}]
L	length of heat pipe [m]
L_a	total adiabatic section length [m]
L_c	condenser length [m]
L_e	evaporator length [m]
$\dot{m}$	mass flow [kg s^{-1}]
P	pressure [N m^{-2}]
q	radial heat flux [W m^{-2}]
R	gas constant [J kg^{-1} K^{-1}]
r	radius coordinate
T	temperature [K]
t_w	wick thickness [m]
u	azimuthal velocity component [m s^{-1}]
v	radial velocity component [m s^{-1}]
w	axial velocity component [m s^{-1}]
w_s	opening width of screen mesh [m]
z	axial coordinate.

Greek symbols

ε	wick porosity
θ	azimuthal coordinate
μ	dynamic viscosity [kg m^{-1} s^{-1}]
ρ	density [kg m^{-3}].

Subscripts

eff	effective
l	liquid
lw	liquid–wick region
o, c	outer wall condenser
o, e	outer wall evaporator
s	solid
v	vapor
w	wick
0	datum.

transfer model. The use of a conjugate model allowed the vapor temperature to be solved for directly instead of being assumed constant. It was further assumed that no boiling occurred within the wick, but evaporation occurred at the liquid/wick interface. Both the elliptic and partially parabolic forms of the conservation equations were examined. The mass, momentum, and energy equations were solved for the velocity, pressure, and temperature fields for the entire heat pipe domain: vapor, liquid–wick, and pipe wall regions in the evaporator, adiabatic transport, and condenser sections. The heat transfer in the liquid–wick region was modeled as pure conduction. Conjugate axial conduction, vapor compressibility, flow reversal, and viscous dissipation effects were discussed.

The objective of this study was to develop a three-dimensional numerical model for determining the temperature, pressure and velocity distributions in the entire domain of a circumferentially-heated and a block-heated heat pipe as a conjugate problem without assuming a uniform vapor temperature [3, 4]. The problem was solved such that the evaporation and condensation occur at the vapor/liquid interface with no boiling within the wick. This assumption is valid for all heat fluxes for high-temperature heat pipes and low heat flux for low-temperature heat pipes. This model was an extension of that developed by Chen and Faghri [1] from two dimensions to three dimensions with the addition of block heating in the evaporator.

2. MATHEMATICAL MODELING

The schematics of the computational domains used for the block-heated and circumferentially-heated heat pipes are shown in Figs. 1 and 2, respectively. The components of velocity in the r, θ, and z directions were v, u, and w, respectively. In the block-heated model, a plane of symmetry along the r and z axes was established so that only half of the heat pipe needed to be modeled.

The flow in the vapor region was considered to be compressible, laminar, and steady. The heat transfer through the liquid–wick region was modeled as pure conduction with no fluid flow by using the effective thermal conductivity of the working fluid and wick material. The properties of the working fluid and wall material were constant and the vapor density of the working fluid followed the perfect-gas law. Evaporation and condensation occurred only at the inner radius of the liquid–wick region. At the liquid–wick/vapor interface, the vapor temperature was calculated using the Clausius–Clapeyron equation. At the liquid–wick/vapor and liquid–wick/wall interfaces, the harmonic mean of the thermal conductivity was used in the energy equation. The elliptic versions of the conservation equations were solved as a one-domain conjugate problem. Gravity and other body force terms were neglected.

Under these assumptions, the conservation equations in the vapor region are [5]

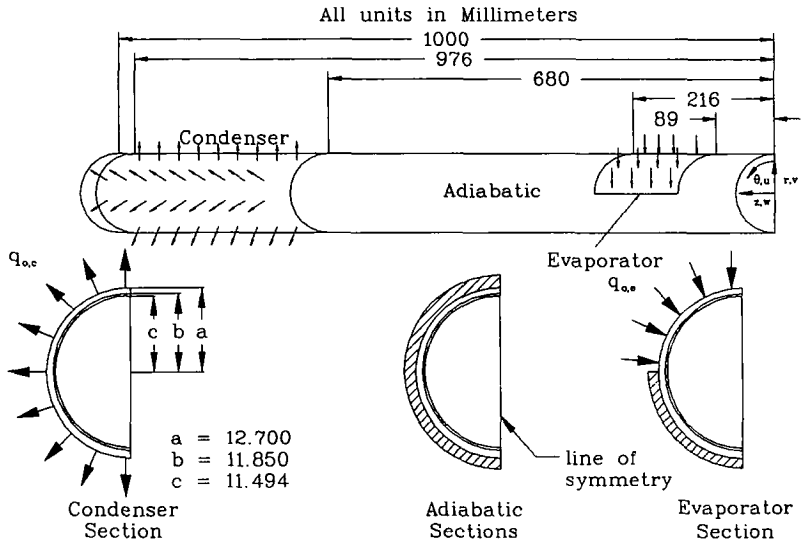

FIG. 1. Block-heated heat pipe model.

mass

$$\frac{1}{r}\frac{\partial}{\partial r}(\rho r v)+\frac{1}{r}\frac{\partial}{\partial \theta}(\rho u)+\frac{\partial}{\partial z}(\rho w)=0 \qquad (1)$$

r-momentum

$$\rho\left(v\frac{\partial v}{\partial r}+\frac{u}{r}\frac{\partial v}{\partial \theta}-\frac{u^2}{r}+w\frac{\partial v}{\partial z}\right)=-\frac{\partial P}{\partial r}$$
$$+\frac{1}{r}\frac{\partial}{\partial r}\left(2r\mu\left[\frac{\partial v}{\partial r}-\frac{1}{3}\left(\frac{1}{r}\frac{\partial}{\partial r}(rv)+\frac{1}{r}\frac{\partial u}{\partial \theta}+\frac{\partial w}{\partial z}\right)\right]\right)$$
$$+\frac{1}{r}\frac{\partial}{\partial \theta}\left(\mu\left[r\frac{\partial}{\partial r}\left(\frac{u}{r}\right)+\frac{1}{r}\frac{\partial v}{\partial \theta}\right]\right)$$
$$-\frac{2\mu}{r^2}\left[\frac{\partial u}{\partial \theta}+v-\frac{1}{3}\left(\frac{\partial}{\partial r}(rv)+\frac{\partial u}{\partial \theta}+r\frac{\partial w}{\partial z}\right)\right]$$
$$+\frac{\partial}{\partial z}\left[\mu\left(\frac{\partial w}{\partial r}+\frac{\partial v}{\partial z}\right)\right] \qquad (2)$$

θ-momentum

$$\rho\left(v\frac{\partial u}{\partial r}+\frac{u}{r}\frac{\partial u}{\partial \theta}+\frac{vu}{r}+w\frac{\partial u}{\partial z}\right)$$
$$=-\frac{1}{r}\frac{\partial P}{\partial \theta}+\frac{1}{r^2}\frac{\partial}{\partial r}\left[r^3\mu\left(\frac{\partial}{\partial r}\left(\frac{u}{r}\right)+\frac{1}{r^2}\frac{\partial v}{\partial \theta}\right)\right]$$
$$+\frac{1}{r}\frac{\partial}{\partial \theta}\left(\frac{2\mu}{r}\left[\frac{\partial u}{\partial \theta}+v-\frac{1}{3}\left(\frac{\partial}{\partial r}(rv)+\frac{\partial u}{\partial \theta}+r\frac{\partial w}{\partial z}\right)\right]\right)$$
$$+\frac{\partial}{\partial z}\left[\mu\left(\frac{\partial u}{\partial z}+\frac{1}{r}\frac{\partial w}{\partial \theta}\right)\right] \qquad (3)$$

z-momentum

$$\rho\left(v\frac{\partial w}{\partial r}+\frac{u}{r}\frac{\partial w}{\partial \theta}+w\frac{\partial w}{\partial z}\right)=-\frac{\partial P}{\partial z}$$
$$+\frac{1}{r}\frac{\partial}{\partial r}\left(r\mu\left[\frac{\partial w}{\partial r}+\frac{\partial v}{\partial z}\right]\right)+\frac{1}{r}\frac{\partial}{\partial \theta}\left[\mu\left(\frac{\partial u}{\partial z}+\frac{1}{r}\frac{\partial w}{\partial \theta}\right)\right]$$
$$+\frac{\partial}{\partial z}\left[2\mu\left(\frac{\partial w}{\partial z}-\frac{1}{3r}\left(\frac{\partial}{\partial r}(rv)+\frac{\partial u}{\partial \theta}+r\frac{\partial w}{\partial z}\right)\right)\right] \qquad (4)$$

energy

$$\rho C_p\left(v\frac{\partial T}{\partial r}+\frac{u}{r}\frac{\partial T}{\partial \theta}+w\frac{\partial T}{\partial z}\right)$$
$$=k_v\left[\frac{1}{r}\frac{\partial}{\partial r}\left(r\frac{\partial T}{\partial r}\right)+\frac{1}{r^2}\frac{\partial^2 T}{\partial \theta^2}+\frac{\partial^2 T}{\partial z^2}\right]$$
$$+2\mu\left[\left(\frac{\partial v}{\partial r}\right)^2+\left[\frac{1}{r}\left(\frac{\partial u}{\partial \theta}+v\right)\right]^2+\left(\frac{\partial w}{\partial z}\right)^2\right]$$
$$+\mu\left[\left(\frac{\partial u}{\partial z}+\frac{1}{r}\frac{\partial w}{\partial \theta}\right)^2+\left(\frac{\partial w}{\partial r}+\frac{\partial v}{\partial z}\right)^2\right.$$
$$\left.+\left[\frac{1}{r}\frac{\partial v}{\partial \theta}+r\frac{\partial}{\partial r}\left(\frac{u}{r}\right)\right]^2\right]$$
$$-\frac{2}{3}\mu\left[\frac{1}{r}\frac{\partial}{\partial r}(rv)+\frac{1}{r}\frac{\partial u}{\partial \theta}+\frac{\partial w}{\partial z}\right]^2$$
$$+v\frac{\partial P}{\partial r}+\frac{u}{r}\frac{\partial P}{\partial \theta}+w\frac{\partial P}{\partial z}. \qquad (5)$$

For the wall and the liquid–wick regions the energy equation simplified to

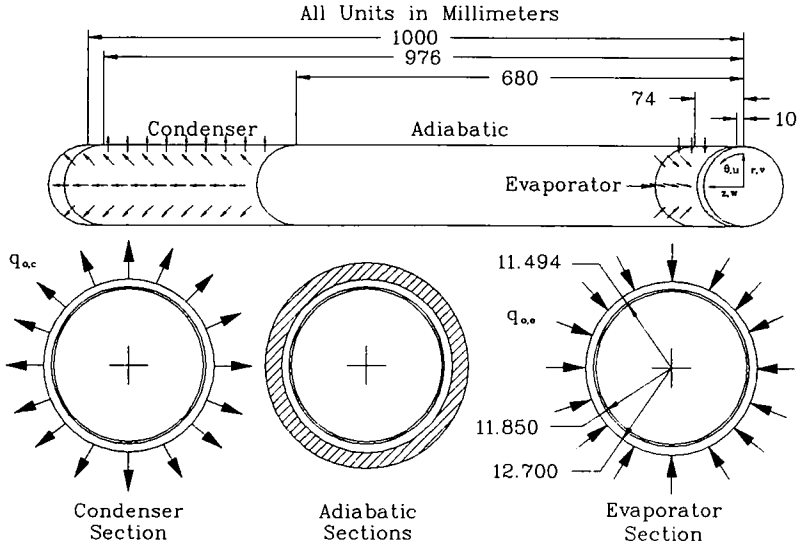

FIG. 2. Circumferentially-heated heat pipe model.

$$\frac{k}{r}\frac{\partial}{\partial r}\left[r\frac{\partial T}{\partial r}\right]+\frac{k}{r^2}\left(\frac{\partial^2 T}{\partial \theta^2}\right)+k\left(\frac{\partial^2 T}{\partial z^2}\right)=0. \quad (6)$$

In the pipe wall, the thermal conductivity in equation (6) is k_s. The effective thermal conductivity for the liquid–wick region, k_{eff}, was calculated for a screen mesh wick as follows [6]:

$$k_{\text{eff}}=\frac{k_l[k_l+k_w-(1-\varepsilon)(k_l-k_w)]}{k_l+k_w+(1-\varepsilon)(k_l-k_w)} \quad (7)$$

where k_l is the thermal conductivity of the liquid and k_w is that of the wick material. The wick porosity in equation (7) was given by Chang [7]

$$\varepsilon=1-\frac{\pi CD}{2(1+C)} \quad (8)$$

where C is the ratio of the wire diameter to the opening width of the screen, and D is the ratio of the wire diameter to the screen thickness.

The Clausius–Clapeyron equation was used to determine the vapor temperature from the saturation vapor pressure at the liquid–wick/vapor interface.

$$T_v=\frac{1}{\frac{1}{T_0}-\frac{R}{h_{fg}}\ln\frac{P_v}{P_0}} \quad (9)$$

where T_0 and P_0 are the reference saturation temperature and pressure imposed at the evaporator end cap. If P_0 is set to a datum pressure, the absolute pressure distribution in the vapor region can be found.

The ideal gas law was needed to solve for the density because of compressibility effects

$$P_v=\rho R T_v. \quad (10)$$

The various boundary condition specifications required for the conservation equations are summarized in Table 1.

3. NUMERICAL SOLUTION PROCEDURE

The circumferentially-heated and block-heated models were solved as a single-domain, convection–conduction problem with three radial regions: pipe wall, liquid–wick, and vapor. The heat transfer through the wall and liquid–wick was treated as pure conduction by neglecting the liquid flow in the wick. To account for the discontinuity in the thermal conductivity at the liquid–wick/wall and the liquid–wick/vapor interfaces, the transport coefficient in the energy equation was evaluated using the harmonic mean of values from each side of the interface [8].

The generalized finite-difference method of solution developed by Spalding [9] was used to solve the elliptic conservation equations with the boundary conditions given in Table 1. The finite-domain equations were derived by integration of the differential conservation equations over a control volume surrounding a grid node. The integrated source term due to viscous dissipation and the pressure term in the energy equation were linearized and the SIMPLEST practice [9] was used to solve the momentum equations. The SIMPLEST method of solution involves guessing the pressure field and then solving the momentum equations to obtain the velocity components. The pressure is then corrected and the entire procedure repeated until convergence is achieved. In SIMPLEST, the momentum finite-difference equations are initially solved using diffusion contributions only. The conduction terms are then added when the pressure distribution is corrected. The hybrid scheme was used to determine the coefficients. When the absolute value of a cell Peclet number was greater than 2, the upwind dif-

Table 1. Boundary conditions for circumferentially-heated and block-heated heat pipe models

	Evaporator ($0 \leqslant z \leqslant L_e$)	Adiabatic ($L_e \leqslant z \leqslant L_e+L_a$)	Condenser ($L_e+L_a \leqslant z \leqslant L$)
Outer pipe wall ($r = r_w$) (circumferential heating)	$0 \leqslant \theta \leqslant 2\pi$: $q_{0,e} = -k_s \frac{\partial T_s}{\partial r} = \text{constant}$	$\frac{\partial T_s}{\partial r} = 0$	$q_{0,c} = -q_{0,e} = -k_s \frac{\partial T_s}{\partial r} = \text{constant}$
Outer pipe wall ($r = r_w$) (block heating)	$0 \leqslant \theta \leqslant \frac{\pi}{2}$: $q_{0,e} = -k_s \frac{\partial T_s}{\partial r} = \text{constant}$; $\frac{\pi}{2} \leqslant \theta \leqslant \pi$: $\frac{\partial T_s}{\partial r} = 0$	$\frac{\partial T_s}{\partial r} = 0$	$q_{0,c} = q_{0,e} \frac{A_e}{A_c} = -k_s \frac{\partial T_s}{\partial r} = \text{constant}$
Wall/liquid–wick interface ($r = r_v + t_w$)	$T_{lw} = T_s, \quad k_s \frac{\partial T_s}{\partial r} = k_{eff} \frac{\partial T_{lw}}{\partial r}$		
Liquid–wick/vapor interface ($r = r_v$)	$w_v = u_v = 0, \quad v = \frac{\dot{m}}{\rho_v}, \quad T_v = \left[\frac{1}{T_0} - \frac{R}{h_{fg}} \ln \frac{P_v}{P_0}\right]^{-1}$; $q = \dot{m} h_{fg} = k_v \frac{\partial T_v}{\partial r} - k_{eff} \frac{\partial T_{lw}}{\partial r}$		
Centerline ($r = 0$) (circumferential heating)	$\frac{\partial u}{\partial r} = \frac{\partial w}{\partial r} = v = \frac{\partial T}{\partial r} = \frac{\partial P}{\partial r} = 0$		
Centerline ($r = 0$) (block heating)	$u = \frac{\partial w}{\partial r}\left(0, \frac{\pi}{2}, z\right) = v = \frac{\partial T}{\partial r}\left(0, \frac{\pi}{2}, z\right) = \frac{\partial P}{\partial r}\left(0, \frac{\pi}{2}, z\right) = 0$		
End caps ($z = 0, L$)	$u = v = w = \frac{\partial T}{\partial z} = 0, \quad P(z = 0) = P_0$		
Periodic	All the dependent variables are assumed to be periodic with a period of 2π		

ferencing scheme was used [8]. Otherwise, a central-difference scheme was used combined with a three-line approximation of the coefficients.

The pressure and temperature terms were solved using a whole-field approach which takes into account the effects from all three directions simultaneously. The velocity components were solved using a slab-by-slab approach in the axial direction. A false time step relaxation factor equal to the average cell transverse time was used to aid in convergence of the velocity components.

The term $\dot{m}h_{fg}$ was added to the source term in the energy balance at the liquid–wick/vapor interface in the evaporator and condenser sections to account for the latent heat of evaporation and condensation. The heat flux at the liquid–wick/vapor interface was assumed to be equal to that at the outer wall for the first 150 iterations, and then corrected to an exact energy balance for the remaining iterations. This was done to reduce the possibility of divergence in the initial iterations.

Convergence was determined by examining the difference in the absolute values of the dependent variables between two successive iterations in a single cell. If the difference was less than 10^{-4}, the cell was considered to be converged. A centerline cell near the condenser end cap was used for this convergence check. Also, when the sum of the absolute volumetric errors over the whole field was less than 10^{-7} and steadily decreasing with increasing iterations, the solution was considered to be converged. In the circumferentially-heated heat pipe model, the number of grids in the axial and radial directions was doubled until the converged solution did not vary by more than 1% with grid size. In the block-heated model, the number of grids in the radial and axial directions were increased by 10% and the azimuthal direction was doubled until the converged solution did not vary with grid size. There was a limitation on the amount of computer memory available for the block-heated model, which was the reason that the number of grids was not doubled in each axis for the grid independence

check. An axial by radial by circumferential grid of $50 \times 34 \times 16$ was used for the circumferentially-heated model and a $50 \times 34 \times 50$ grid was used for the block-heated model for the final numerical results presented in this study.

4. RESULTS AND DISCUSSION

The numerical model developed for this study for the two different heating distributions was examined for a 100 W heat input. The outer wall temperatures from both models were compared with experimental wall temperatures. Excellent agreement was found between the experimental data and the numerical models. The axial component of the velocity at several axial locations was compared between the two heating modes. The outer wall temperature, and centerline pressure and Mach number for the circumferentially-heated model were compared with the two-dimensional model developed by Chen and Faghri [1]. The radial and circumferential components of the velocity in the block-heated model were examined and the existence of swirling flow was discovered.

5. CIRCUMFERENTIALLY-HEATED HEAT PIPE MODEL

A 100 W heat input was specified in the evaporator of the circumferentially-heated copper–water heat pipe model. Figure 3 shows the wall temperature, centerline pressure, and centerline Mach number comparisons between the present three-dimensional model and the numerical results given by Chen and Faghri [1]. Wall temperature measurements from the experimental set-up discussed in Part I are also shown for comparison. The agreement is excellent between the three-dimensional and two-dimensional models in all three figures. This was expected due to the symmetry of the model in the azimuthal direction. Figure 3(a) shows the outer wall temperatures along the top of the experimental heat pipe and the numerical model. The difference between the numerical wall temperatures and the experimental data in the condenser section was due to the simplifying assumption of uniform heat removal in the numerical model. Figure 3(b) shows the relative pressure distribution. The reference pressure at the evaporator end cap was fixed to zero. If the operating pressure at the evaporator end cap is added to this pressure distribution, the actual pressure profile can be found.

Two opposite azimuthal grids were used in Fig. 4 to show the symmetry of the velocity profile about the centerline at various axial locations. Figure 4(a) shows the axial variation of the velocity profile in the region around the evaporator section. As expected, the velocity profile was symmetric about the heat pipe centerline and the magnitude increased from the evaporator end cap due to the addition of mass from evaporation. Figure 4(b) shows the axial variation of the velocity profile in the middle of the adiabatic section. The flow field appears to be fully developed in this section. There was little or no change in the velocity profile in the axial grids about the center of the adiabatic region. Figure 4(c) shows the velocity profile in the condenser section of the heat pipe model, which also shows the symmetry of the velocity profile about the centerline. The magnitude of the velocity profile was reduced as the amount of vapor decreases due to condensation. Vapor flow reversal occurred near the liquid–wick/vapor interface, which was caused by the significant amount of pressure recovery.

Figure 5 shows the outer wall temperature profile along the circumferentially-heated model, which was uniform around the circumference. The wall temperature quickly dropped along the axial direction in the region around the center of the evaporator. The wall temperature in the adiabatic section was uniform in the axial direction throughout most of its length. The condenser had the coldest wall temperatures which were uniform in the axial direction except at the beginning and the end.

6. BLOCK-HEATED HEAT PIPE MODEL

The numerical results of the block-heated heat pipe model were compared with experimental data taken from the block-heated copper–water heat pipe (Part I) with a heat input of 100 W. Figure 6(a) shows the experimental outer wall temperatures along the top of the heat pipe compared with the numerical model. The agreement between the numerical model and the experimental data was excellent except in the condenser section. These differences were again due to the assumption of a uniform heat flux in the condenser of the numerical model. The relative pressure distribution at the centerline is shown in Fig. 6(b). Because the velocity profile was asymmetric in the circumferential direction, the pressure profile was also asymmetric about the centerline. The circumferential location taken for the centerline in Fig. 6(b) is the same as the one examined in the circumferentially-heated model (Fig. 3(b)). The fluctuations in the pressure near the condenser end cap were due to the significant variations in the vapor velocity due to swirling.

Figure 7(a) shows the axial variation of the velocity vector profile in the region around the evaporator. From the evaporator end cap to the heated region, the axial component was symmetric about the heat pipe centerline because conjugate heat conduction tends to spread the heat over the entire circumference. From the beginning of the heated region to the condenser end cap, the location of the maximum velocity shifted toward the bottom of the heat pipe. This was due to the blowing in the evaporator section at the top of the heat pipe model.

The axial variation of the velocity profile near the center of the adiabatic section is given in Fig. 7(b).

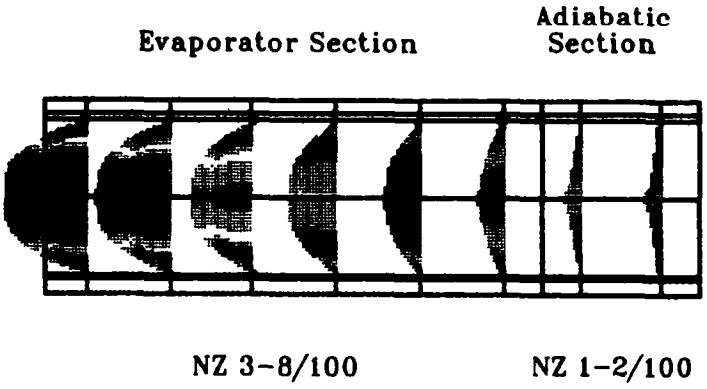

(a) Evaporator Section

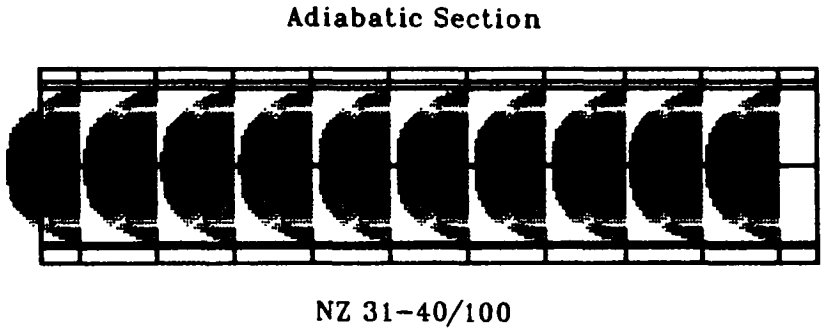

(b) Adiabatic Section

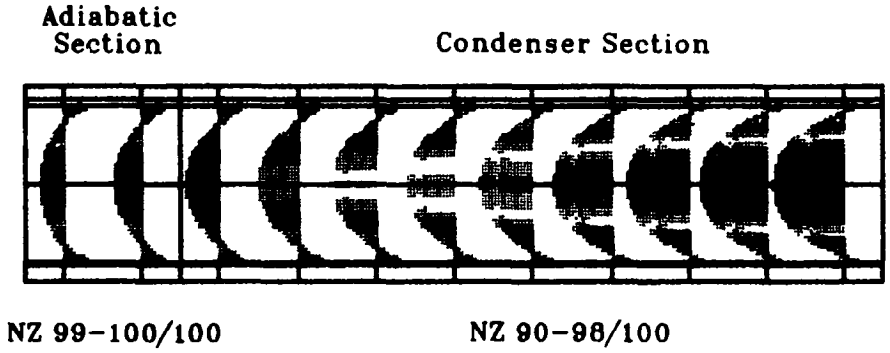

(c) Condenser Section

FIG. 4. Axial variation of velocity for the circumferentially-heated heat pipe, Q = 100 W.

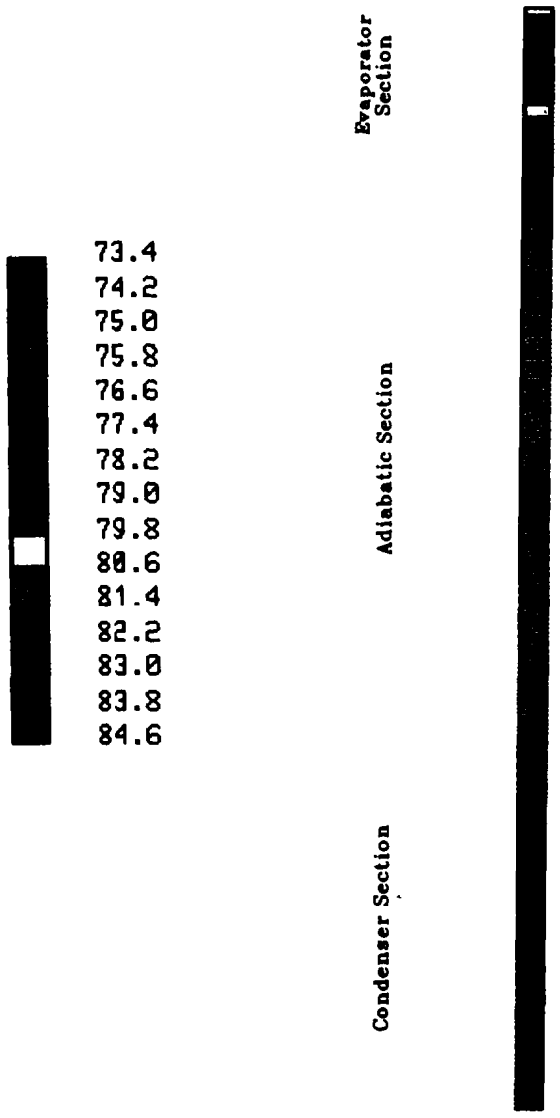

FIG. 5. Outer wall temperature for the circumferentially-heated heat pipe (°C), $Q = 100$ W.

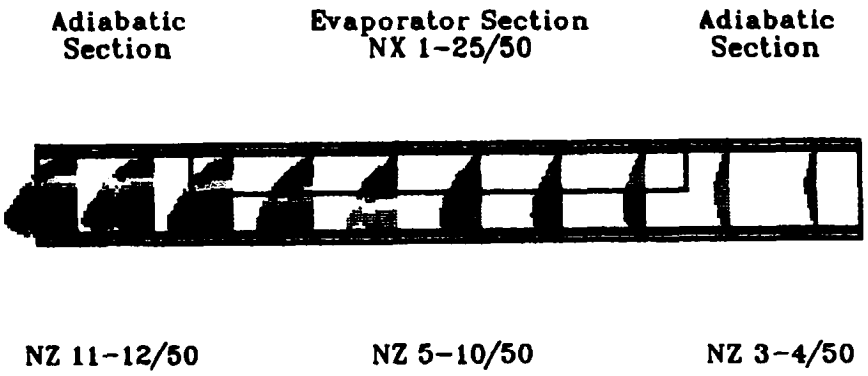

(a) Evaporator Section

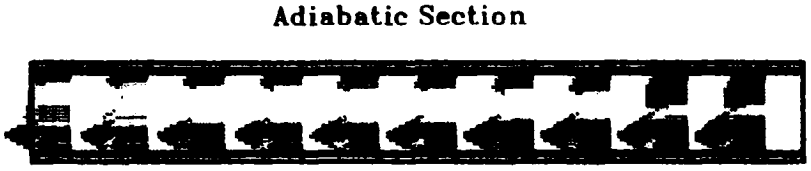

(b) Adiabatic Section

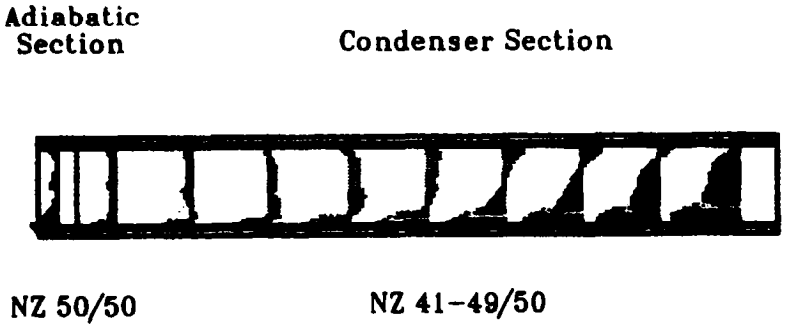

(c) Condenser Section

FIG. 7. Axial variation of velocity for the block-heated heat pipe model, $Q = 100$ W.

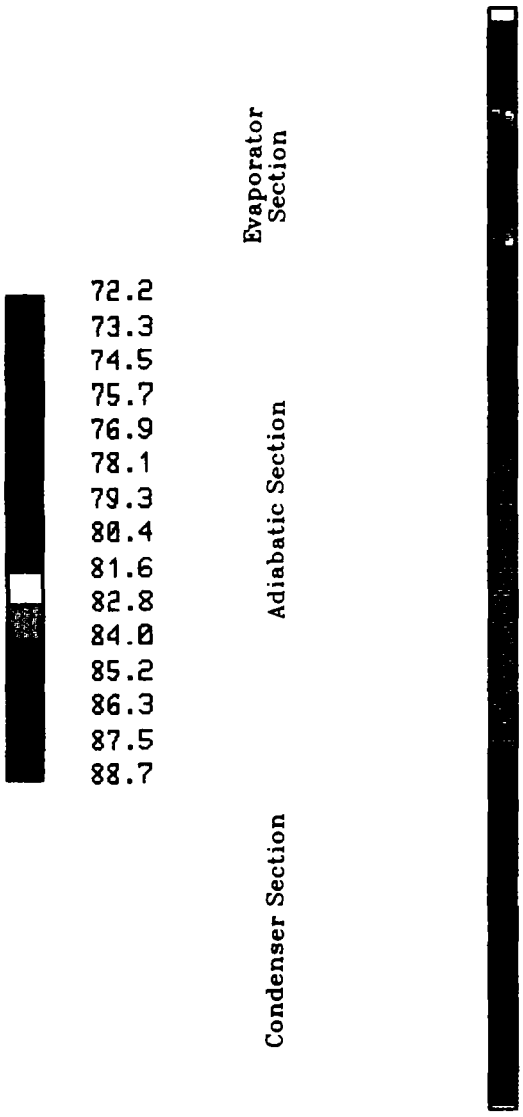

FIG. 8. Outer wall temperatures for the block-heated heat pipe model (C), $Q = 100$ W.

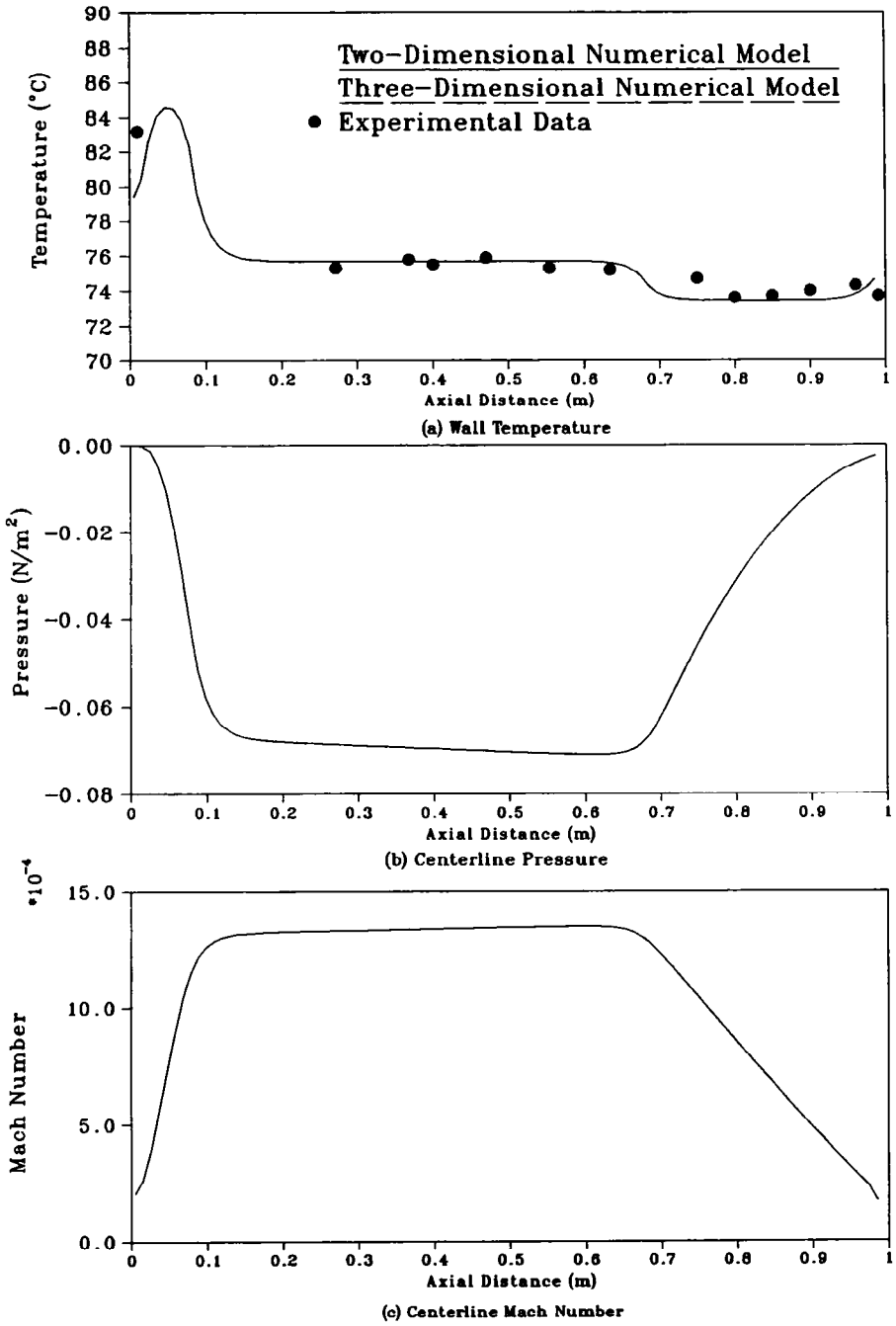

FIG. 3. Circumferentially-heated heat pipe, $Q = 100$ W.

Unlike the circumferentially-heated model, the velocity profile peak changed slightly in both magnitude and location over the length of the adiabatic region. The vapor velocity field began to exhibit a significant amount of swirling which started in the heated region and grew as the flow moved away from the evaporator end cap. This swirling caused considerable asymmetry in the velocity profile in the condenser section. The swirling will be shown and discussed in more detail in Figs. 9–11.

Figure 7(c) shows the axial variation of the velocity profile near the condenser end cap. Because the swirling was dispersed throughout the vapor region, there was no smooth transition in the velocity profile from the top to the bottom of the model in the last six axial grids.

When comparing Figs. 4 and 7, significant differences were found between the circumferentially-heated and the block-heated models. The circumferentially-heated heat pipe velocity profile was

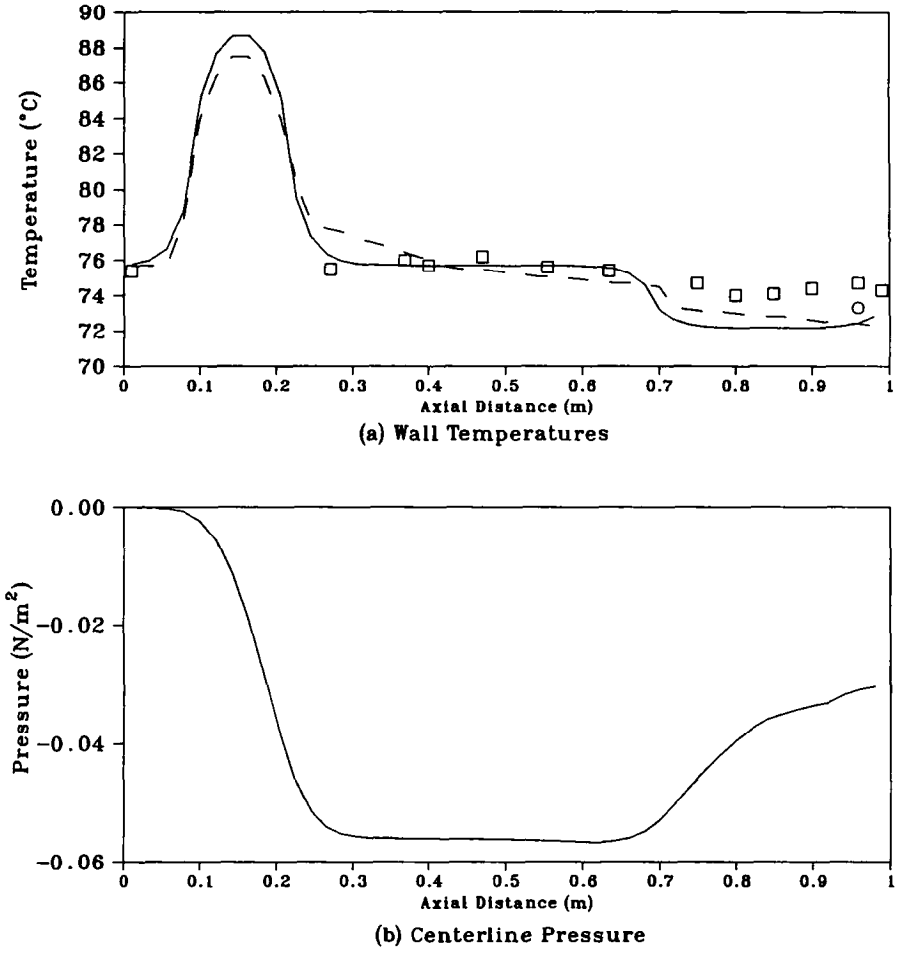

FIG. 6. Block-heated heat pipe, $Q = 100$ W.

symmetric about the centerline of the model and was fully developed in the adiabatic region. This was shown by the lack of significant changes in the velocity profile through several axial locations in the adiabatic section (Fig. 4(b)). The block-heated model shows no symmetry about the centerline except for the small adiabatic section between the evaporator end cap and the heated region. Even in the condenser section of the block-heated model, the flow remains asymmetric, with most of the reverse flow taking place at the top of the vapor space. The blowing from the block heater causes the vapor flow to move to the bottom of the vapor region and the length of the pipe was insufficient for the flow field to develop to a symmetric flow about the centerline.

Figure 8 shows the wall temperature of the block-heated heat pipe model. The heat pipe wall temperature was symmetric in the azimuthal direction throughout most of its length, except in the region about the block heater.

Figures 9–11 present the radial and circumferential components of the velocity vector as seen looking down the pipe axis. Figure 9(a) is from the first axial grid of the evaporator section of the block-heated heat pipe model. Along the top half of the model, the blowing representing the evaporation of the working fluid from the heated region was present. In conjunction with Fig. 7(a), it was determined that the majority of the vapor from the blowing region flowed around the circumference to the bottom and then down the length of the heat pipe.

Figure 9(b) is from the second grid in the evaporator section. The flow field was similar to that in Fig. 9(a) except for the appearance of a small amount of

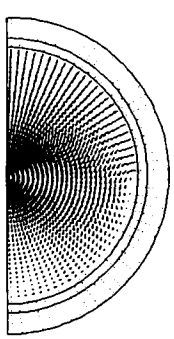

(a) NZ 5/50

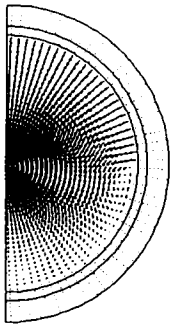

(b) NZ 6/50

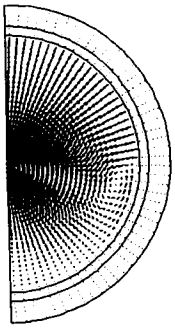

(c) NZ 8/50

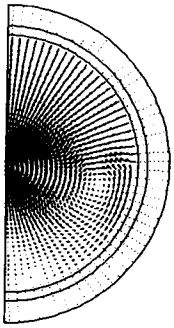

(d) NZ 10/50

FIG. 9. Velocity variation in the radial and circumferential directions in the evaporator section of the block-heated heat pipe model, $Q = 100$ W.

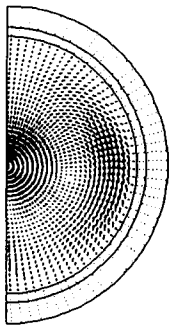

(a) NZ 11/50

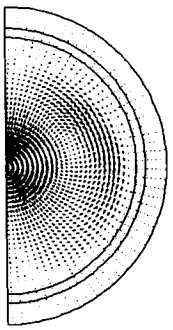

(b) NZ 15/50

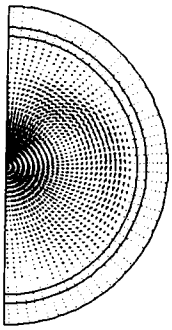

(c) NZ 20/50

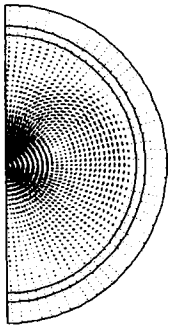

(d) NZ 25/50

FIG. 10. Velocity variation in the radial and circumferential directions in the adiabatic section of the block-heated heat pipe model, $Q = 100$ W.

counterclockwise swirling in the vapor flow field near the liquid–wick/vapor interface, just below the point where the heated region and the insulated region meet. Further down the heat pipe, this swirling encompassed an increasing amount of the vapor region. Figure 9(c) is from the middle of the evaporator section. The flow field followed the same general pattern as in Figs. 9(a) and (b), but the area of swirling grew in size and magnitude. Figure 9(d) is from the end of the evaporator section. The swirling developed even more and affected about half the vapor radius in the region near the circumferential point where the heater and insulated regions meet.

Figure 10(a) is from the first axial grid of the adiabatic section. With the elimination of most of the blowing along the top of the vapor region, the swirling moved into the top half of the model. Even though most of the flow field was affected by the swirling, the first and last grids in the circumferential direction were not, and so when viewed from the side (Fig. 7(a)) a smooth transition from the top to the bottom of the model still appeared in the velocity flow field.

Figure 10(b) is from a few grids further from the evaporator than Fig. 10(a). From this axial location onwards, the swirling affected the entire vapor region. The magnitude of the swirling had a profound effect on the location of the maximum velocity. Figure 10(c) is an axial view of the radial and circumferential components of the velocity at the middle of the adiabatic section. The center of the swirling migrated into the top half of the vapor space. Figure 10(d) is at the end of the adiabatic section. The swirling continued to grow in magnitude and became more uniform about the vapor space. The center of the swirling shifted slightly towards the top of the pipe.

Figure 11(a) is at the beginning of the condenser section. The uniform suction about the circumference of the liquid–wick/vapor interface can be seen in this figure. The swirling lost some of its momentum from the axial location shown in Fig. 10(d). This was caused by the removal of mass from the vapor region. Figure 11(b) is from the middle of the condenser section. Although the swirling had lost considerable magnitude, it was still significant at this location. The magnitude of the swirling was no longer uniform about the vapor space. Near the liquid–wick/vapor interface, the magnitude of the swirling was much higher than at the centerline. This nonuniformity in the swirling caused significant variation in the axial component of the velocity. Figure 11(c) is at the end of the condenser. The center of the swirling had disappeared, but there still was a significant component of the swirling in the vapor space. The remaining effects of the swirling caused the major part of the reversed flow shown in

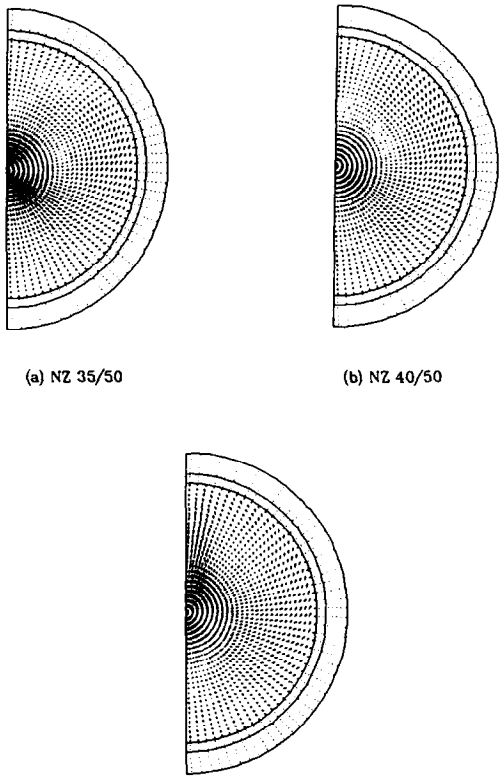

FIG. 11. Velocity variation in the radial and circumferential directions in the condenser section of the block-heated heat pipe model, $Q = 100$ W.

Fig. 7(c) to move to the top of the vapor region. The swirling observed in the numerical model of the block-heated heat pipe was caused by end effects in the circumferential direction at the heater edge.

7. CONCLUSIONS

Three-dimensional numerical models of a circumferentially-heated and a block-heated heat pipe were developed. The wall temperatures from both models were compared with experimental data with excellent agreement. The vapor velocity profiles for block heating were examined and compared with the profiles of the circumferential heating model.

The numerical vapor velocity profiles showed the symmetric nature of the circumferentially-heated heat pipe about the centerline. In the same regions of the block-heated heat pipe, the vapor flow first moves radially away from the heater with only a small portion turning axially before it reaches the far side. It is also shown that there are significant end effects at the edge of the block heater. These caused a significant amount of swirling, which greatly increased the asymmetric nature of the vapor flow. Although the maximum axial velocities of the two models were almost the same, the location of the maximum axial component was significantly different. The maximum velocity of the circumferentially-heated heat pipe occurred at the centerline, whereas the location of the maximum velocity for the block-heated heat pipe stayed near the liquid–wick/vapor interface opposite the heated section. The flow reversal showed that the pressure recovery in the circumferentially-heated heat pipe occurred near the liquid–wick/vapor interface, but in the block-heated heat pipe it occurred near the plane of symmetry.

Acknowledgement—Funding for this work was provided by a joint effort of the NASA Lewis Research Center and Thermal Energy Group of the Aero Propulsion Laboratory of the U.S. Air Force under contract F33615-89-C-2820.

REFERENCES

1. M. M. Chen and A. Faghri, An analysis of the vapor flow and the heat conduction through the liquid–wick and pipe wall in a heat pipe with single and multiple heat sources, *Int. J. Heat Mass Transfer* **33**, 1945–1955 (1990).
2. Y. Cao and A. Faghri, A transient two-dimensional compressible analysis for high temperature heat pipes with a pulsed heat input, *Numer. Heat Transfer* **18A**, 483–502 (1990).
3. J. H. Rosenfeld, Modeling of heat transfer into a heat pipe for a localized heat input zone, *Proc. A.I.Ch.E. Symp. Series, Heat Transfer* **83**, 71–76 (1987).
4. Y. Cao, A. Faghri and E. T. Mahefkey, The thermal performance of heat pipes with localized heat input, *Int. J. Heat Mass Transfer* **32**, 1279–1287 (1989).
5. E. N. Ganic, J. P. Hartnett and W. M. Rohsenow, *Handbook of Heat Transfer Fundamentals*. McGraw-Hill, New York (1985).
6. S. W. Chi, *Heat Pipe Theory and Practice; A Sourcebook*. McGraw-Hill, New York (1976).
7. W. S. Chang, Porosity and effective thermal conductivity of wire screens, *ASME J. Heat Transfer* **112**, 5–9 (1990).
8. S. V. Patankar, *Numerical Heat Transfer and Fluid Flow*. McGraw-Hill, New York (1980).
9. D. B. Spalding, Mathematical modeling of fluid-mechanics, heat transfer, and chemical reaction processes, a lecture course, CFDU Report, HTD/80/1, Imperial College, London, U.K. (1980).